Article

Hollowing Sn-Doped TiO Nanospheres via Ostwald Ripening

Jing Li, and Hua Chun Zeng

J. Am. Chem. Soc., **2007**, 129 (51), 15839-15847 • DOI: 10.1021/ja073521w

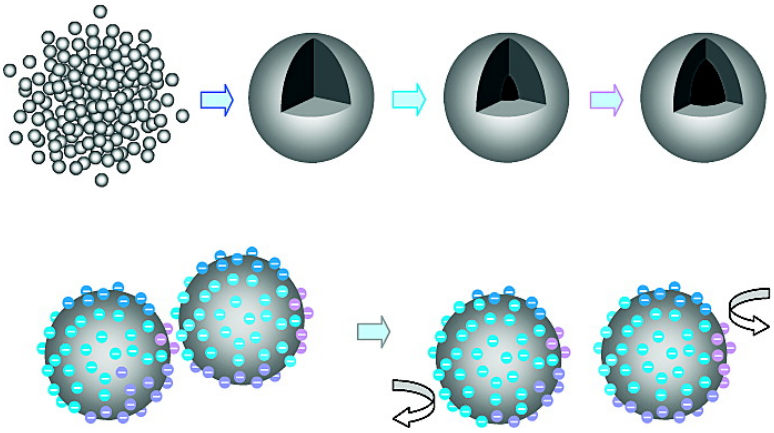

J|A|C|S
ARTICLES
Published on Web 11/30/2007

Hollowing Sn-Doped TiO_2 Nanospheres via Ostwald Ripening

Jing Li[†] and Hua Chun Zeng*[,†,‡]

Department of Chemical and Biomolecular Engineering and Minerals, Metals, and Materials Technology Center, Faculty of Engineering, National University of Singapore, 10 Kent Ridge Crescent, Singapore 119260

Received May 17, 2007; E-mail: chezhc@nus.edu.sg

Abstract: The well-known physical phenomenon Ostwald ripening in crystal growth has been widely employed in template-free fabrication of hollow inorganic nanostructures in recent years. Nevertheless, all reported works so far are limited only to stoichiometric phase-pure solids. In this work we describe the first investigation of doped (nonstoichiometric) materials using Ostwald ripening as a means of creating interior space. In particular, we chose the $x SnO_2-(1-x)TiO_2$ binary system to establish preparative principles for this approach in synthesis of structurally and compositionally complex nanomaterials. In this study, uniform Sn-doped TiO_2 nanospheres with hollow interiors in 100% morphological yield have been prepared with an aqueous inorganic route under hydrothermal conditions. Furthermore, our structural and surface analyses indicate that Sn^{4+} ions can be introduced linearly into TiO_2, and preferred structural phase(s) can also be attained (e.g., either anatase or rutile, or their mixtures). Fluoride anions of starting reagents are adsorbed on the surface sites of oxygen. The resultant anion overlayer may contribute to stabilization of surface and creation of repulsive interaction among the freestanding nanospheres. On the basis of these findings, we demonstrate that Ostwald ripening can now be employed as a general hollowing approach to architect interior spaces for both simple and complex nanostructures.

Introduction

In recent years, synthetic fabrication of discrete inorganic nanostructures with an interior space has aroused significant attention.[1−12] This type of chemical approach normally makes use of various templating methodologies. For example, micelles and vesicles, sol−gel networks, colloidal polymeric and silica beads, sacrificial metal templates, and even gas bubbles, etc., have been utilized.[3−12] Apart from templating synthesis, recent development in the field is also directed to template-free processes. In particular, various known physical phenomena, such as oriented attachment,[13−15] Ostwald ripening,[16] and Kirkendall effect,[17−19] have been employed in many wet fabrications of hollow inorganic nanostructures.[7,20−39] Among them, mass transport via Ostwald ripening has been proven to be a facile approach to generate symmetric and/or asymmetric interior spaces, including core−shell spaces and multiple shell spaces, for inorganic nanostructures.[22−39] Upon ripening, interior spaces can be created in accordance to matter state and agglomerative pattern of pristine crystallites. For example, smaller, less crystalline, or less dense particles in a colloidal

[†] Department of Chemical and Biomolecular Engineering.
[‡] Minerals, Metals, and Materials Technology Center.

(1) Sun, Y.; Xia, Y. *Science* **2002**, *298*, 2176−2179.
(2) Goldberger, J.; He, R.; Lee, S.; Zhang, Y.; Yan, H.; Choi, H.; Yang, P. *Nature* **2003**, *422*, 599−602.
(3) Sun, Y.; Mayers, B.; Xia, Y. *Adv. Mater.* **2003**, *15*, 641−646.
(4) Bao, J.; Liang, Y.; Xu, Z.; Si, L. *Adv. Mater.* **2003**, *15*, 1832−1835.
(5) Peng, Q.; Dong, Y.; Li, Y. *Angew. Chem., Int. Ed.* **2003**, *42*, 3027−3030.
(6) Yang, Z.; Niu, Z.; Lu, Y.; Hu, Z.; Han, C. C. *Angew. Chem., Int. Ed.* **2003**, *42*, 1943−1945.
(7) Yin, Y.; Rioux, R. M.; Erdonmez, C. K.; Hughes, S.; Somorjai, G. A.; Alivisatos, A. P. *Science* **2004**, *304*, 711−714.
(8) Sun, Y.; Xia, Y. *Adv. Mater.* **2004**, *16*, 264−268.
(9) Yang, H. G.; Zeng, H. C. *Angew. Chem., Int. Ed.* **2004**, *43*, 5206−5209.
(10) Pan, Y.; Huo, K.; Hu, Y.; Fu, J.; Lu, Y.; Dai, Z.; Hu, Z.; Chen, Y. *Small* **2005**, *1*, 1199−1203.
(11) Nakashima, T.; Kimizuka, N. *J. Am. Chem. Soc.* **2003**, *125*, 6386−6387.
(12) Guo, C.-W.; Cao, Y.; Xie, S.-H.; Dai, W.-L.; Fan, K.-N. *Chem. Commun.* **2003**, 700−701.
(13) Penn, R. L.; Banfield, J. F. *Am. Mineral.* **1998**, *83*, 1077−1082.
(14) Penn, R. L.; Banfield, J. F. *Science* **1998**, *281*, 969−971.
(15) Penn, R. L. *J. Phys. Chem. B* **2004**, *108*, 12707−12712.
(16) Ostwald, W. *Z. Phys. Chem.* **1900**, *34*, 495−503.
(17) Kirkendall, E.; Thomassen, L.; Upthegrove, C. *Trans. AIME* **1939**, *133*, 186−203.
(18) Kirkendall, E. O. *Trans. AIME* **1942**, *147*, 104−110.
(19) Smigelskas, A. D.; Kirkendall, E. O. *Trans. AIME* **1947**, *171*, 130−142.
(20) Yang, H. G.; Zeng, H. C. *Angew. Chem., Int. Ed.* **2004**, *43*, 5930−5933.
(21) Liu, B.; Zeng, H. C. *J. Am. Chem. Soc.* **2004**, *126*, 8124−8125.
(22) Yang, H. G.; Zeng, H. C. *J. Phys. Chem. B* **2004**, *108*, 3492−3495.
(23) Zeng, H. C. *J. Mater. Chem.* **2006**, *16*, 649−662.
(24) Chang, Y.; Teo, J. J.; Zeng, H. C. *Langmuir* **2005**, *21*, 1074−1079.
(25) Zhang, Y.; Li, G.; Wu, Y.; Luo, Y.; Zhang, L. *J. Phys. Chem. B* **2005**, *109*, 5478−5481.
(26) Liu, B.; Zeng, H. C. *Small* **2005**, *1*, 566−571.
(27) Li, J.; Zeng, H. C. *Angew. Chem., Int. Ed.* **2005**, *44*, 4342−4345.
(28) Teo, J. J.; Chang, Y.; Zeng, H. C. *Langmuir* **2006**, *22*, 7369−7377.
(29) Wang, Y.; Zhu, Q.; Zhang, H. *Chem. Commun.* **2005**, *41*, 5231−5233.
(30) Zheng, Y.; Cheng, Y.; Wang, Y.; Zhou, L.; Bao, F.; Jia, C. *J. Phys. Chem. B* **2006**, *110*, 8284−8288.
(31) Cao, X.; Gu, L.; Zhuge, L.; Gao, W.; Wang, W.; Wu, S. *Adv. Funct. Mater.* **2006**, *16*, 896−902.
(32) Li, B.; Rong, G.; Xie, Y.; Huang, L.; Feng, C. *Inorg. Chem.* **2006**, *45*, 6404−6410.
(33) Zhang, H.; Qi, L. *Nanotechnology* **2006**, *17*, 3984−3988.
(34) Xu, H.; Wang, W.; Zhu, W.; Zhou, L. *Nanotechnology* **2006**, *17*, 3649−3654.
(35) Lou, X. W.; Wang, Y.; Lee, J. Y.; Archer, L. A. *Adv. Mater.* **2006**, *18*, 2325−2329.
(36) Yu, J.; Guo, H.; Davis, S. A.; Mann, S. *Adv. Funct. Mater.* **2006**, *16*, 2035−2041.
(37) Wang, W.-S.; Zhen, L.; Xu, C.-Y.; Zhang, B.-Y.; Shao, W.-Z. *J. Phys. Chem. B* **2006**, *110*, 23154−23158.
(38) Huang, J.; Gao, L. *J. Am. Ceram. Soc.* **2006**, *89*, 3887−3880.
(39) Cheng, Y.; Wang, Y.; Jia, C.; Bao, F. *J. Phys. Chem. B* **2006**, *110*, 24399−24402.

aggregate will be dissolved gradually, while larger, better crystallized, or denser particles in the same aggregate are growing.[22,26] It should be mentioned that, at the present stage of development, the method is only limited to simple monometallic oxides, hydroxides, sulfides, or stoichiometric transition-metal tetraoxometalates, although a large variety of hollow materials, such as CuO, Cu_2O, TiO_2, SnO_2, Fe_2O_3, Co_3O_4, $Ni(OH)_2$, CuS, ZnS, $CdMoO_4$, and $ZnWO_4$, etc., have been prepared.[22−39] In order to widen its application to more complex material systems, such as binary or even ternary metal (mixed) oxides and sulfides, some fundamental issues should be addressed. In this connection, it should be pointed out that synthetic complexity will be increased when more complex product compositions are targeted, especially when both morphological and architectural controls are demanded. For instance, matter relocation during prolonged processes, which is indispensable in the ripening, may also result in undesired secondary phase formation or phase separation if starting solid precursors become compositionally complicated.

To pursue the above research, applicability of this approach must be established urgently. In this article, therefore, we chose a binary oxide system, Sn-doped TiO_2 (i.e., $xSnO_2-(1-x)TiO_2$ solid solution), as a first attempt to address this issue. With the increase in compositional complexity, binary oxides may possess novel physicochemical properties that their primitive mono-oxides do not have. For example, it has been widely recognized that the efficiency of photocatalytic reactions of ion-doped TiO_2-based materials can be improved substantially owing to modification of their band-gap energy structures and introduction of dopant energy states.[40] Thus far, many ionic dopants in different valence states have been investigated, including both metallic ions (e.g., Ca^{2+}, Sr^{2+}, Ba^{2+}, Al^{3+}, Ga^{3+}, Cr^{3+}, Fe^{3+}, Co^{3+}, Ce^{3+}, Ln^{3+}, Sn^{4+}, Zr^{4+}, Nb^{5+}, Mo^{5+}, Sb^{5+}, and Ta^{5+}) and nonmetallic ions (e.g., N^{3+}, C^{4+}, S^{4+}, F^-, Cl^-, and Br^-).[40] Particularly, doping Sn^{4+} into TiO_2-based catalysts in replacing some of Ti^{4+} cations has been demonstrated to be a good routine to increase the reaction rate in the photoassisted degradation of various organic compounds and pollutants.[41−52] In preparing the Sn-doped TiO_2 photocatalysts, several methods such as coprecipitation, sol−gel and hydrothermal syntheses, and chemical vapor deposition have been commonly adopted. It is noted that except for the hydrothermal method, the materials prepared by these methods all require high-temperature treatments in order to obtain good product crystallinity. Furthermore, although their size could be small, the binary oxide products are normally polydisperse with very wide ranges of size distribution.[41−52] To the best of our knowledge, morphological control and uniformity of the nanoparticles for the Sn-doped TiO_2 materials have not yet been achieved.

In this article, we report an aqueous synthetic scheme for preparation of monodisperse Sn-doped TiO_2 nanospheres. With hydrolysis of fluoride salts of both TiF_4 and SnF_4, uniform Sn-doped TiO_2 nanospheres with an interior can be fabricated in 100% morphological yield via Ostwald ripening. Formation of spherical morphology for the binary oxides can be attributed to the presence of nonmetallic anions used in synthesis. More importantly, for the first time, we demonstrate that Ostwald ripening can also be used as a facile wet chemical route to synthesize binary metal oxide nanospheres with additional architecture of interior spaces.

Experimental Section

Preparation of starting solutions of titanium tetrafluoride TiF_4 (40 mM) used in this work followed a similar method detailed in our previous report.[53] In the preparation of tin tetrafluoride SnF_4 solutions, the following method was developed. Briefly, deionized water was used as a solvent to dissolve the metal fluoride salt. Prior to solution preparation, the deionized water was first adjusted to pH 2.0 using an HCl solution (1.5 M) to avoid rapid hydrolysis. In a typical process, for example, 0.22 g of SnF_4 powder was added to 100 mL of the acidified deionized water and continuously stirred for 1 h. Because SnF_4 has a very low solubility in water at room temperature, the powder added could not be totally dissolved. This solute−solvent system was kept still at room temperature for at least 1 day to allow a slow dissolving process, although undissolved SnF_4 could still be observed. The upper supernatant, i.e., clear saturated SnF_4 aqueous solution, was then used in our materials synthesis. On the other hand, it was also observed that SnF_4 could also undergo hydrolysis reaction and condense into solid SnO_2 upon solution aging, and therefore, the prepared solution was used within the first 5 days after its preparation. The solutions prepared in this way have a nominal SnF_4 concentration (e.g., 11.3 mM in this example). To be more specific, they are also labeled with a shelf time (i.e., 1−5 days) in this report since actual concentrations of solution could be a function of time.

In a typical synthesis, 0−2 mL of the above TiF_4 solution (40 mM) and 0−4 mL of SnF_4 solution (11.3 mM (nominal), 1−5 days after preparation) were mixed with deionized water (pH 7) to reach a total volume of 30 mL in a Teflon-lined stainless steel autoclave. After that, hydrothermal synthesis was conducted at 180 °C for 2−8 h in an electric oven. White solid products (i.e., tin-doped titanium dioxide, $Ti_{1-x}Sn_xO_{1-0.5y}F_y$, Table 1) were harvested by centrifuging and washing extensively with deionized water.

The crystallographic information of the as-prepared samples was established using powder X-ray diffraction (XRD, Shimadzu X-ray diffractometer, model 6000, Cu Kα radiation $\lambda = 1.5406$ Å) at a scanning rate of 2° min^{-1}. Crystal morphology and lattice structural information of the products were obtained with various microscopy and diffraction methods. In particular, studies with field emission scanning electron microscopy (FESEM), transmission electron microscopy (TEM), high-resolution transmission electron microscopy (HR-TEM), and selected area electron diffraction (SAED) were carried out on JSM-6700F, JEM-2010, and JEM-2010F microscopes, respectively. Furthermore, bulk and surface compositional analyses for the prepared samples were performed with energy-dispersive X-ray spectroscopy (EDX/TEM JEM-2010) and X-ray photoelectron spectroscopy (XPS,

(40) (a) Carp, O.; Huisman, C. L.; Reller, A. *Prog. Solid State Chem.* **2004**, *32*, 33−177. (b) Kitiyanan, A.; Ngamsinlapasathian, S.; Pavasupree, S.; Yoshikawa, S. *J. Solid State Chem.* **2005**, *178*, 1044−1048. (c) Dürr, M.; Rosselli, S.; Yasuda, A.; Nelles, G. *J. Phys. Chem. B* **2006**, *110*, 21899−21902.
(41) Tian, H.; Ma, J.; Huang, X.; Xie, L.; Zhao, Z.; Zhou, J.; Wu, P.; Dai, J.; Hu, Y.; Zhu, Z.; Wang, H.; Chen, H. *Mater. Lett.* **2005**, *59*, 3059−3061.
(42) Fresno, F.; Guillard, C.; Coronado, J. M.; Chovelon, J. −M.; Tudela, D.; Soria, J.; Herrmann, J.-M. *J. Photochem. Photobiol. A: Chem.* **2005**, *173*, 13−20.
(43) Fresno, F.; Coronado, J. M.; Tudela, D.; Soria, J. *Appl. Catal. B* **2005**, *55*, 159−167.
(44) Fresno, F.; Tudela, D.; Coronado, J. M.; Fernández-García, M.; Hungría, A. B.; Soria, J. *Phys. Chem. Chem. Phys.* **2006**, *8*, 2421−2430.
(45) Fresno, F.; Tudela, D.; Maira, A. J.; Rivera, F.; Coronado, J. M.; Soria, J. *Appl. Organomet. Chem.* **2006**, *20*, 220−225.
(46) Fernández-García, M.; Martínez-Arias, A.; Fuerte, A.; Conesa, J. C. *J. Phys. Chem. B* **2005**, *109*, 6075−6083.
(47) Jing, L.; Fu, H.; Wang, B.; Wang, D.; Xin, B.; Li, S.; Sun, J. *Appl. Catal. B* **2006**, *62*, 282−291.
(48) Uchiyama, H.; Imai, H. *Chem. Commun.* **2005**, 6014−6016.
(49) Mahanty, S.; Roy, S.; Sen, S. *J. Cryst. Growth* **2004**, *261*, 77−81.
(50) Lin, J.; Yu, J. C.; Lo, D.; Lam, S. K. *J. Catal.* **1999**, *183*, 368−372.
(51) Demetry, C.; Shi, X. *Solid State Ionics* **1999**, *118*, 271−279.
(52) Luo, H.; Takata, T.; Lee, Y.; Zhao, J.; Domen, K.; Yan, Y. *Chem. Mater.* **2004**, *16*, 846−849.
(53) Yang, H. G.; Zeng, H. C. *J. Phys. Chem. B* **2003**, *107*, 12244−12255.

Table 1. EDX Analytical Results and Structural Analysis (Tetragonal Unit Cell Constants a_0 and c_0) for the Samples Reported in Figure 5[a]

sample	chemical formula	a_0 (Å)	c_0 (Å)	TiF_4 (mL)	SnF_4 (mL)	[MF_4] (mM)	Sn/Ti (atomic)	F/Ti (atomic)	F/Sn (atomic)
a	$TiO_{1.99}F_{0.03}$	3.79	9.51	2.0	0	2.67		0.03	
b	$Ti_{0.94}Sn_{0.06}O_{1.94}F_{0.12}$	3.79	9.55	2.0	0.4	2.82	0.06	0.13	2.26
c	$Ti_{0.88}Sn_{0.12}O_{1.90}F_{0.19}$	4.63	2.97	2.0	0.9	3.01	0.14	0.22	1.56
d	$Ti_{0.83}Sn_{0.17}O_{1.90}F_{0.20}$	4.64	2.98	2.0	1.4	3.20	0.21	0.24	1.17
e	$Ti_{0.78}Sn_{0.22}O_{1.88}F_{0.23}$	4.65	3.00	2.0	2.0	3.42	0.28	0.30	1.08
f	$Ti_{0.63}Sn_{0.37}O_{1.92}F_{0.16}$	4.66	3.00	2.0	4.0	4.17	0.59	0.26	0.45
g	$SnO_{1.94}F_{0.12}$	4.73	3.19	0	4.0	1.51			0.12

[a] [MF_4] is total concentration of both TiF_4 and SnF_4 in starting precursor solutions (30 mL).

AXIS-HSi, Kratos Analytical), respectively. The binding energies (BEs) of XPS spectra of all studied elements were referred to the C 1s photoelectron peak arising from adventitious carbon (i.e., BE of C 1s was set at 284.6 eV). The UV−vis absorption spectra of suspensions of some representative oxide samples (Table 1) were measured by a UV−vis−NIR scanning spectrophotometer (Shimadzu, model UV-3101 PC, with ethanol as a solvent).

Results and Discussion

Figure 1 is a series of TEM images showing morphological evolution of the oxide nanospheres. With a short reaction time (2 h, a−c) the crystallite aggregates give a spherical morphology. On the basis of these images it is understandable that the nanospheres undergo a hollowing process when the aging time is prolonged (4 h, d−f). The solid evacuation is much more pronounced after 8 h of the reactive aging (g−i). The formed hollow spheres are quite uniform with a 100% morphological yield. We also find that during the hollowing process the size of these nanospheres does not change much. For example, the nanospheres in Figure 1 have an average size of about 329 ± 25, 320 ± 19, and 352 ± 24 nm over reaction/processing times of 2, 4, and 8 h, respectively. This observation illustrates that the hollowing process is essentially similar to what has been known in the preparation of pure anatase TiO_2 hollow spheres.[22] Owing to the hydrolysis reactions of the fluoride salt precursors ($MF_4 + 2H_2O \rightarrow MO_2 + 4HF$, where M = Ti and Sn), numerous small metal oxide crystallites nucleate from solution

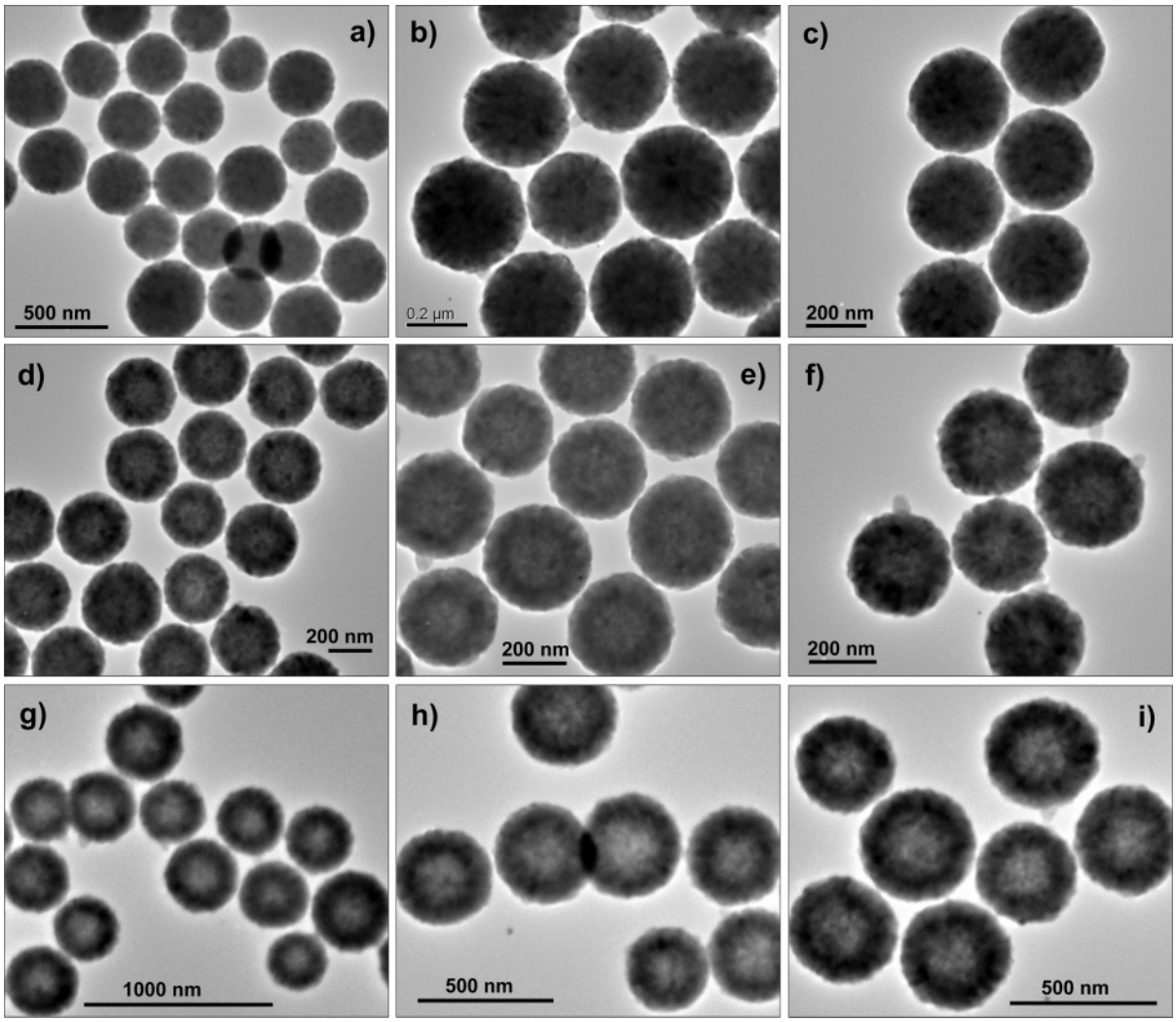

Figure 1. Evolution of $Ti_{1-x}Sn_xO_{1-0.5y}F_y$ nanospheres upon reaction time: (a−c) 2, (d−f) 4, and (g−i) 8 h. Reaction conditions: 2 mL of 40 mM TiF_4 + 26.6 mL of H_2O + 1.4 mL of 11.3 mM SnF_4 (5 days after its preparation) at 180 °C for 2−8 h (see Experimental Section).

under hydrothermal conditions and quickly congregate to spherical aggregates in order to decrease their surface energies. It should be mentioned that this initial solid phase might not be well crystallized owing to rapid spontaneous nucleation, and thus, Ostwald ripening dictates growth and recrystallization after hydrolysis. During this process the inner crystallites, which had a higher surface energy, would dissolve and transfer out, producing channels connecting inner space and outer space in the oxide shells. The hollow interior of the mixed oxide spheres was also investigated with the FESEM method for broken spheres, which affirmed the above TEM findings (Supporting Information, SI-1).

The SnF_4 solution used in the samples of Figure 1 was kept still for 5 days after preparation. A similar experiment was also conducted using a SnF_4 solution, which was prepared after only 1 day, as reported in Figure 2. No distinguishable difference can be found under the same experimental conditions. Therefore, we verify a shelf time of 1−5 days for SnF_4 solution adopted in our synthesis (see Experimental Section). Once again, the central hollow interior can be clearly identified in the TEM image (Figure 2a). The FESEM images in this figure also demonstrate that the nanospheres are discretely freestanding with a uniform size distribution across a large sampling area.

The crystal structures of the above Sn-doped TiO_2 products (1.4 mL of SnF_4, Figure 1 (5 days) and Figure 2 (1 day)) were further investigated with the XRD method (similar to the curve d (3 days), Figure 5). All peaks can be indexed to the tetragonal rutile phase (SG, $P4_2/mnm$; JCPDS no. 21-1276). It has been found that Sn^{4+} doping induces an increment of lattice constants a_0 and c_0 of rutile TiO_2 unit cell due to a larger ionic radius of Sn^{4+} (which will be discussed together with other samples in Figure 5 and Table 1). This structural expansion has also been observed with the HRTEM technique. In particular, the images of lattice fringe in Figure 3a and b show interplanar distances of $d_{111} = 2.27$ Å and $d_{110} = 3.33$ Å, respectively, in this rutile phase. The SAED pattern in Figure 3c indicates that the Sn-doped TiO_2 nanospheres are polycrystalline and the most distinct five concentric diffraction rings can be assigned to (110), (101), (111), (211), and (301) planes from the center, sequentially. Due to replacement with tin cations in the nanospheres and related lattice expansion, the measured $d_{111} = 2.27$ Å and $d_{110} = 3.33$ Å are in fact intermediate values between those of rutile TiO_2 and SnO_2, referring to the same interplanar distances of $d_{111} = 2.19$ Å and $d_{110} = 3.25$ Å for the phase pure rutile TiO_2 and $d_{111} = 2.31$ Å and $d_{110} = 3.35$ Å for the phase pure SnO_2.[54−57] Furthermore, EDX spectroscopic results reported in Table 1 reveal that this rutile sample is detected with significant quantities of Sn^{4+} and F^- at atomic ratios of Sn/Ti = 0.21 and F/Ti = 0.24, respectively (synthesized with 1.4 mL of SnF_4, sample d).

The content of tin in the mixed oxide solutions has also been investigated in detail. Displayed in Figure 4 is a set of TEM images of the Sn-doped TiO_2 nanospheres prepared with a different volume ratio of TiF_4 and SnF_4 precursor solutions, and the corresponding XRD patterns of these samples can be found, respectively, in Figure 5. All the diffraction peaks are shifting toward to lower 2-theta side upon increasing SnF_4 content in synthesis, indicating a gradual expansion of the crystal lattice of rutile TiO_2 phase when Sn^{4+} ions are incorporated into the lattice under the studied conditions; the corresponding lattice constants of these samples are tabulated in Table 1. When no SnF_4 was added to the starting solution, the as-prepared TiO_2 nanospheres are in anatase phase (pattern a, Figure 5, SG, $I4_1/amd$; $a_0 = 3.79$ Å and $c_0 = 9.51$ Å; JCPDS no. 21-1272) exhibiting a hollow interior in the center. When 0.4 mL of SnF_4

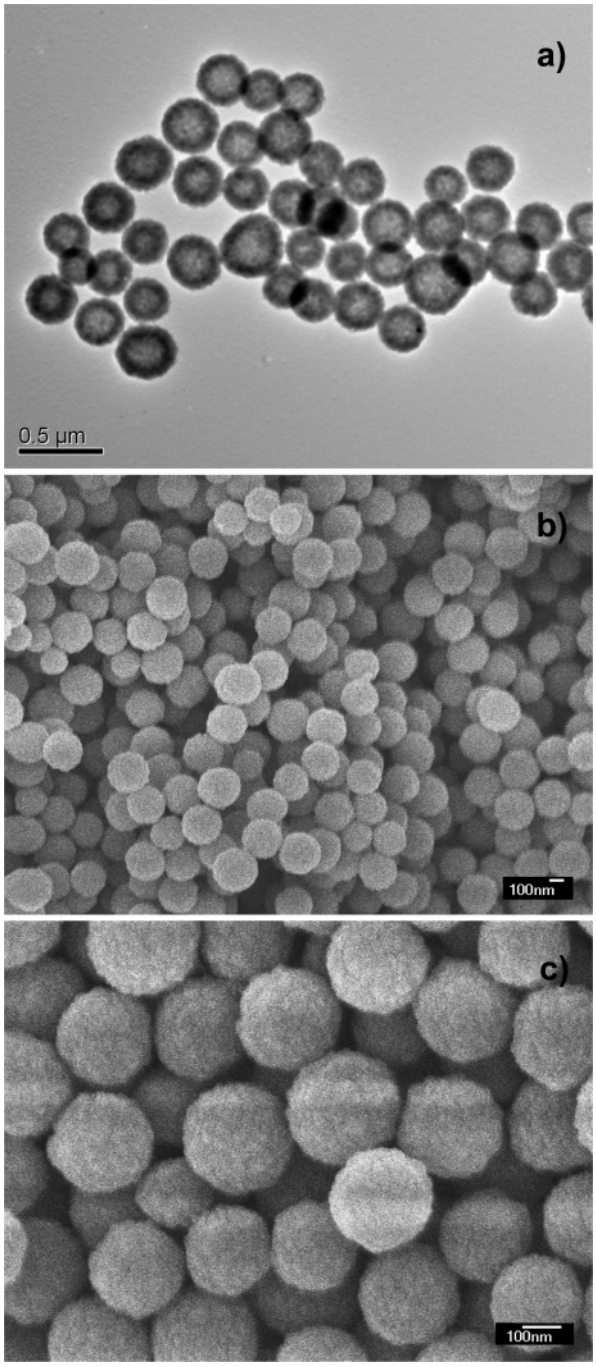

Figure 2. Panoramic views of $Ti_{1-x}Sn_xO_{1-0.5y}F_y$ nanospheres (a, TEM image, b and c, FESEM images). Reaction conditions: 2 mL of 40 mM TiF_4 + 26.6 mL of H_2O + 1.4 mL of 11.3 mM SnF_4 (1 day after its preparation) at 180 °C for 8 h (see Experimental Section).

(54) Hu, Y.-S.; Kienle, L.; Guo, Y.-G.; Maier, J. *Adv. Mater.* **2006**, *18*, 1421−1426.
(55) Falcomer, D.; Daldosso, M.; Cannas, C.; Musinu, A.; Lasio, B.; Enzo, S.; Speghini, A.; Bettinelli, M. *J. Solid State Chem.* **2006**, *179*, 2452−2457.
(56) Bakardjieva, S.; Stengl, V.; Szatmary, L.; Subrt, J.; Lukac. J.; Murafa, N.; Niznansky, D.; Cizek. K.; Jirkovsky, J.; Petrova, N. *J. Mater. Chem.* **2006**, *16*, 1709−1716.
(57) Bickley, R. I.; Gonzalez-Carreno, T.; Lees, J. S.; Palmisano, L.; Tilley, R. J. D. *J. Solid State Chem.* **1991**, *92*, 178−190.

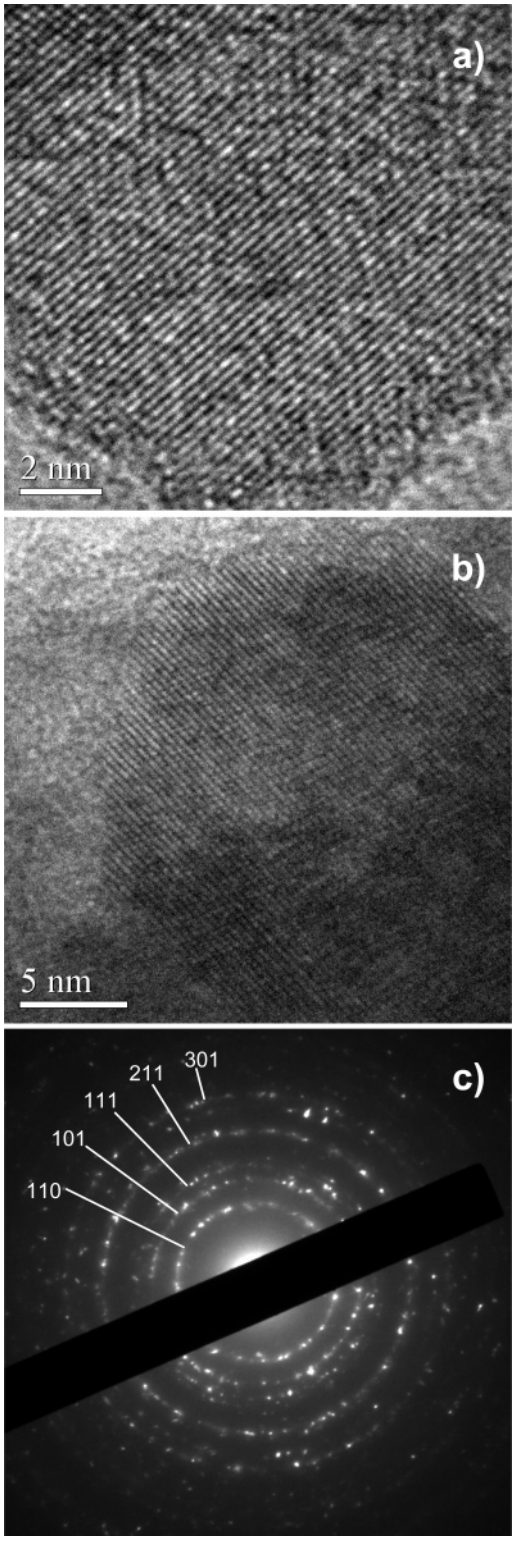

Figure 3. HRTEM images of $Ti_{1-x}Sn_xO_{1-0.5y}F_y$ nanospheres (a and b) and a representative SAED pattern of $Ti_{1-x}Sn_xO_{1-0.5y}F_y$ nanospheres (c). The sample used herein is from that of Figure 2.

was added, the Sn-doped oxide spheres decrease their size to about 400 nm but little central spaces can be observed. From the XRD pattern of this sample (pattern b, Figure 5), we also see a decrease of crystallinity, compared with the product without adding SnF_4, although their main peaks can be still indexed to the anatase phase. With a further increase in the starting SnF_4 solution to 0.9 mL, the anatase phase of oxide nanospheres was changed to a rutile phase (pattern c, Figure 5). These nanospheres have an even smaller average diameter of about 200−250 nm. The Sn-doped TiO_2 products received from the syntheses with 2 and 4 mL of the SnF_4 solution maintain a similar spherical morphology, and they are still in the rutile phase. It is interesting to note that a small solid core exists in the central space, especially for the sample prepared with 4 mL of the SnF_4 precursor solution. It is important to recognize that the phase separation in these samples did not take place under the preparative conditions, i.e., even with a prolonged aging. Finally, we investigated the synthesis of pure SnO_2 nanospheres (synthesized without adding TiF_4). The product SnO_2 in a rutile phase (pattern g, Figure 5; SG, $P4_2/mnm$; $a_0 = 4.73$ Å and $c_0 = 3.19$ Å; JCPDS no. 41-1445) has a quasi-spherical morphology, noting that a central core or two are also present in the hollow interior. Some samples shown in Figure 5 were further investigated with the UV−vis spectrophotometric method for their optical band-gap energies. The measurement method for the optical band-gap energies can be found in the Supporting Information (SI-2). Indeed, undoped TiO_2 (sample a) in pure anatase phase has an optical band-gap energy of 3.22 eV. With inclusion of a small amount of Sn-dopant (sample b), this energy is raised to 3.35 eV, while the same anatase phase is still maintained. When more Sn^{4+} ions are included, the crystal structure of these mixed oxide nanospheres is transformed to rutile phases. However, once again, the optical band-gap energies of the oxide nanospheres are still increased with the content of Sn^{4+} ions. For example, samples c and d in Figure 5 (refer to Table 1) have optical band-gap energies of 3.08 and 3.15 eV, respectively. The observed trend in modification of band-gap energy with Sn^{4+} ions is consistent with the literature data,[48,49] which have been ascribed to shifting the conduction band toward higher energy direction.[48]

Table 1 reports EDX results of the above oxide products. Clearly, the compositions of nanospheres can be controlled by varying the ratio of starting TiF_4 and SnF_4. At a fixed volume of TiF_4 (e.g., 2.0 mL) while changing the volume of reactant SnF_4 (from 0.4 to 4.0 mL), the atomic ratio of Sn/Ti in the resultant products shows a linear relationship with the amount of SnF_4 added in the reactions, as shown in Figure 6. It should be mentioned that Sn cations in samples a−e act as a dopant. Because the size and properties of the dopant (Sn) are different from those of matrix cations (Ti), inclusion of Sn in the final products are more difficult compared to Ti, resulting in lower contents than those in the initial solutions. Fluoride anions, on the other hand, are adsorbed on the surface of the oxide nanospheres (which will be reported shortly in Figure 7), and they show a different trend from that of the lattice-incorporated metal cations. When no SnF_4 is added, for example, fluorine shows a negligible amount of F/Ti = 0.03 in the anatase TiO_2 (Table 1). With an increase in SnF_4 in synthesis, adsorption of fluoride ions first increases and then decreases with a maxima of F/Ti = 0.30 over the studied samples. When tin becomes more dominant in the rutile oxides (e.g., Sn/Ti = 0.59, sample f), the F/Ti ratio decreases again. Consistent with this observation, the fluorine content in the rutile SnO_2 nanospheres is also rather limited (F/Sn = 0.12) when no TiF_4 was present in synthesis. Since the fluoride ions carry negative charges, it is believed that they will replace oxygen anions in order to

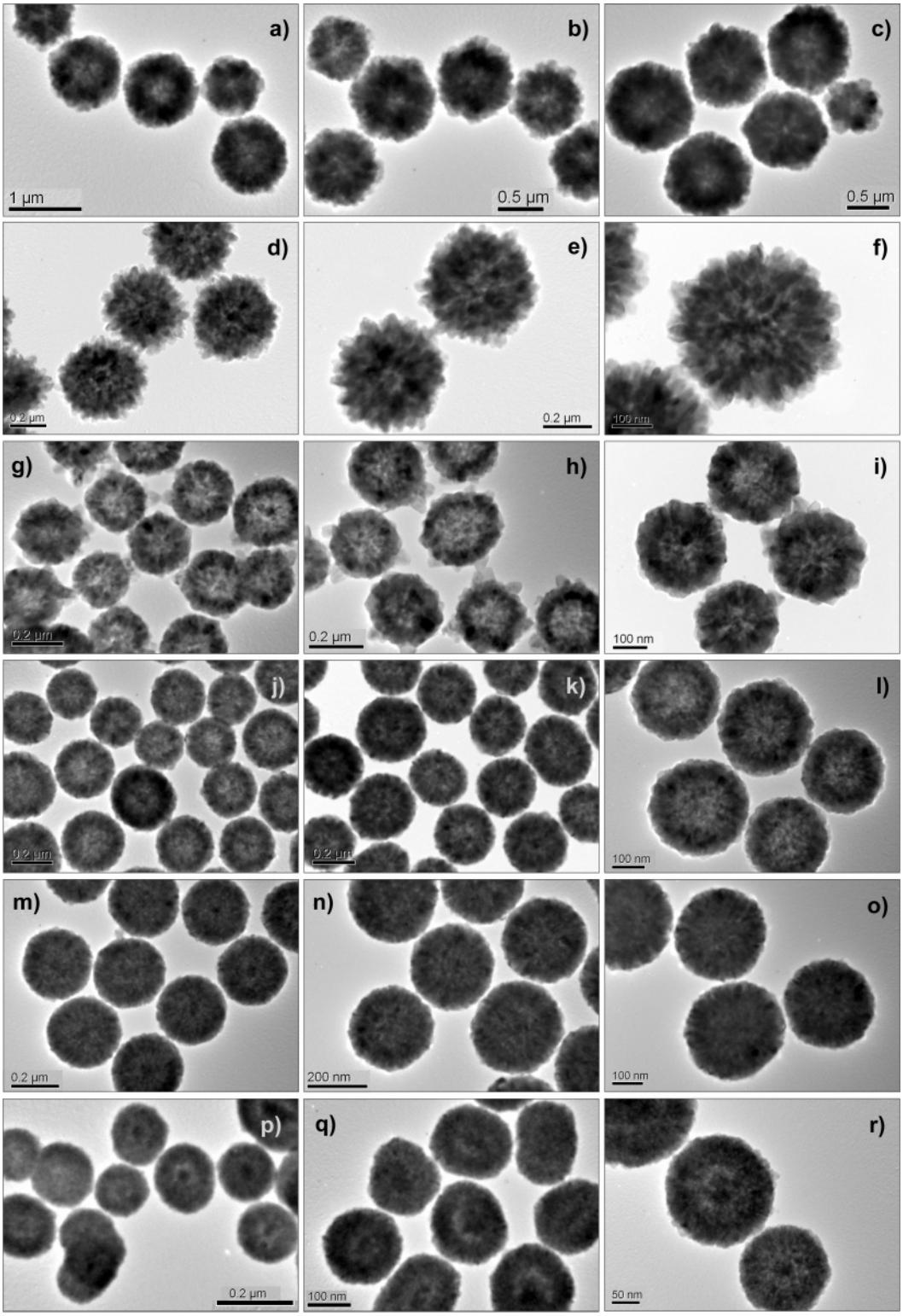

Figure 4. $Ti_{1-x}Sn_xO_{1-0.5y}F_y$ nanospheres synthesized at 180 °C for 8 h with different amounts of SnF_4: (a−c) 2 mL of TiF_4 + 28 mL of H_2O, (d−f) 2 mL of TiF_4 + 27.6 mL of H_2O + 0.4 mL of SnF_4, (g−i) 2 mL of TiF_4 + 27.1 mL of H_2O + 0.9 mL of SnF_4, (j−l) 2 mL of TiF_4 + 26 mL of H_2O + 2 mL of SnF_4, (m−o) 2 mL of TiF_4 + 24 mL of H_2O + 4 mL of SnF_4, and (p−r) 4 mL of SnF_4 + 26 mL of H_2O ([TiF_4] = 40 mM and [SnF_4] = 11.3 mM (3 days after its preparation)).

compensate for oxygen defects.[58] Therefore, it seems that the over the range of Sn/Ti = 0.06−0.28 surface oxygen defects are increasingly generated in view of the increasing trend observed for the adsorbed fluoride anions over this range.

Using the surface-sensitive analytical technique XPS we found that the fluoride anions are indeed adsorbed only on the surface region. For example, F 1s peaks of all three representative samples (TiO_2, Sn-doped TiO_2, and SnO_2 nanospheres) are located at 684.2 eV, as displayed in Figure 7 (NB, all XPS peak intensities in this figure are in arbitrary units, although the

(58) Minero, C.; Mariella, G.; Maurino, V.; Pelizzetti, E. *Langmuir* **2000**, *16*, 2632−2641.

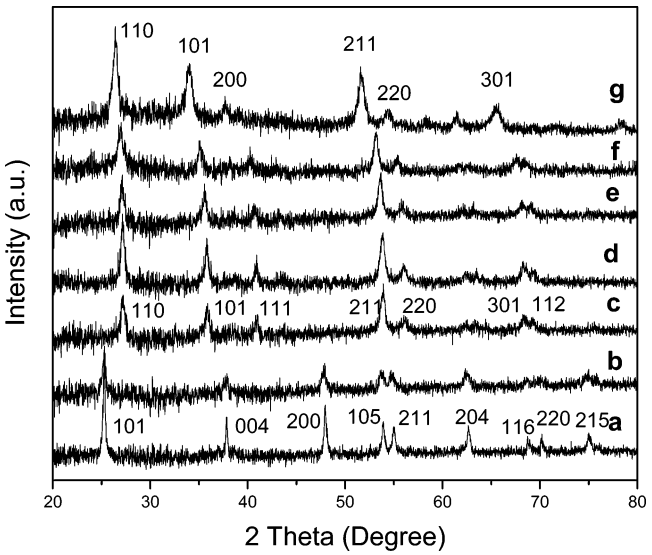

Figure 5. XRD patterns for the $Ti_{1-x}Sn_xO_{1-0.5y}F_y$ nanospheres synthesized at 180 °C for 8 h with different amounts of SnF_4: (a) 2 mL of TiF_4 + 28 mL of H_2O, (b) 2 mL of TiF_4 + 27.6 mL of H_2O + 0.4 mL of SnF_4, (c) 2 mL of TiF_4 + 27.1 mL of H_2O + 0.9 mL of SnF_4, (d) 2 mL of TiF_4 + 26.6 mL of H_2O + 1.4 mL of SnF_4, (e) 2 mL of TiF_4 + 26 mL of H_2O + 2 mL of SnF_4, (f) 2 mL of TiF_4 + 24 mL of H_2O + 4 mL of SnF_4, and (g) 4 mL of SnF_4 + 26 mL of H_2O ([TiF_4] = 40 mM and [SnF_4] = 11.3 mM (3 days after its preparation)). Morphologies of these samples can be found in Figure 4; note that the sample labels are different in Figures 4 and 5.

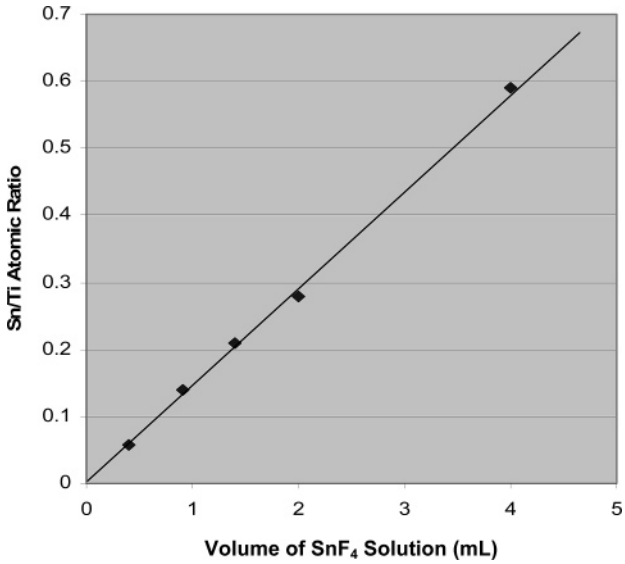

Figure 6. Linear correlation between the atomic ratio of Sn/Ti and starting volume of SnF_4 solution used in synthesis (see Experimental Section and Table 1).

apparent intensities of curves a and b are weaker than that of the c). This F 1s binding energy indicates the presence of F^- ions on the surface region of our prepared oxide nanospheres (i.e., formation of ≡M−F surface species, where M represents both Sn and Ti).[59−61] According to the literature data, the typical F 1s peak of doped F^- (i.e., lattice fluoride anions) in TiO_2 should be located at around 688.5 eV.[59−61] Since the binding energies of the two fluoride species are well separated and can be determined easily with XPS, the presence of lattice fluoride ions in these oxides can be ruled out unambiguously.

Compared to the undoped anatase TiO_2 (sample a, Figure 7), the two peaks of the Ti 2p spectrum for the Sn-doped rutile TiO_2 (sample b, Figure 7) show a small positive shift, which suggests a certain electron drain from the Ti^{4+} in the oxide matrix due to the presence of Sn^{4+}. Consistent with this, the Sn 3d spectrum of the same doped sample reveals a negative shift of 0.5 eV toward lower binding energy compared to those of SnO_2 (sample c, Figure 7).[47] Indeed, this type of charge transfer occurring between two cationic species has been well investigated with XPS for many mixed oxides, where the metallic ions are mixed at an atomic level, forming a heterogeneous linkage of $M_{(A)}-O-M_{(B)}$ (where $M_{(i)}$ represents different metallic species).[62−65] Depending on the cation charge and electronegativity of the element, the electron cloud will be transferred from one type of cation to the other through their oxygen bridge in the linkage structure. In the present case, electron transfer is expected to take place from Ti^{4+} to Sn^{4+},[62−65] considering their difference in electronegativity (Sn = 1.96 vs Ti = 1.54). Therefore, the above complementary binding energy shifts confirm that the two types of metal cations are indeed mixed at the atomic level, in good agreement with our XRD findings in Figure 5.

The O 1s spectrum for anatase TiO_2 (sample a) can be deconvoluted to three peaks. The large peak at 529.8 eV is assigned to lattice oxygen in this oxide phase, while the two peaks located at 531.6 and 532.6 eV could be attributed to Ti−OH (or CO_3^{2-}) and C−OH (or C−O−C) surface species,[66,67] respectively, owing to the residual surfactants on this sample. In sample c the characteristic peak at 530.8 eV is also assigned to lattice oxygen in SnO_2, while the other two peaks positioned at 532.0 and 533.0 eV should be ascribed to surface hydroxyl groups Sn−OH and chemisorbed H_2O molecules,[68] respectively. In the Sn-doped TiO_2 nanospheres (sample b), as expected, lattice oxygen from of the phase pure TiO_2 and SnO_2 is no longer observed, confirming that there is no separate simple oxides in this product. The binding energy of this lattice oxygen in the Sn-doped TiO_2 is located at 530.1 eV, which is in fact between 529.8 (sample a) and 530.8 eV (sample c) observed for the two phase pure oxides,[69] owing to the variation in electronegativities of the two metal elements. Once again, this observation affirms formation of a Sn−O−Ti linkage in the mixed oxide spheres. The remaining two O 1s peaks of sample b at 531.6 and 532.4 eV are attributed to the same chemical constituents as those assigned for the pure phase TiO_2, while the peak at 533.5 eV is assigned to the surface-adsorbed H_2O.[70] Compared to the phase pure TiO_2 and SnO_2 (samples a and c), the peak intensity of lattice oxygen (530.1 eV) in the Sn-doped TiO_2 nanospheres becomes much weaker, suggesting that this oxide surface is also covered with other adsorbates due to replacement of some lattice oxygen. Indeed, consistent with this

(59) Yu, J. C.; Yu, J.; Ho, W.; Jiang, Z.; Zhang, L. *Chem. Mater.* **2002**, *14*, 3808−3816.
(60) Huang, D.-G.; Liao, S.-J.; Dang, Z. *Acta Chim. Sin.* **2006**, *64*, 1805−1811.
(61) Li, D.; Haneda, H.; Labhsetwar, N. K.; Hishita, S.; Ohashi, N. *Chem. Phys. Lett.* **2005**, *401*, 579−584.
(62) Barr, T. L. *J. Vac. Sci. Technol. A* **1991**, *9*, 1793−1805.
(63) Barr, T. L.; Lishka, M. A.; Chen, L. M.; Mohsenian, M. *J. Am. Chem. Soc.* **1988**, *110*, 7962−7975.
(64) Teo, S. H.; Zeng, H. C. *J. Phys. Chem. B* **2001**, *105*, 9093−9100.
(65) Zhu, J.; Chen, F.; Zhang, J.; Chen. H.; Anpo, M. *J. Photochem. Photobiol. A: Chem.* **2006**, *180*, 196−204.
(66) Xu, R.; Zeng, H. C. *Langmuir* **2004**, *20*, 9780−9790.
(67) Chang, Y.; Lye, M. L.; Zeng, H. C. *Langmuir* **2005**, *21*, 3746−3748.
(68) Tala-Ighil, R.; Boumaour, M.; Belkaïd, M. S.; Maallemi, A.; Melhani, K.; Iratni, A. *Solar Energy Mater. Solar Cells* **2006**, *90*, 1797−1814.
(69) Chen, D.; Gao, L. *J. Colloid Interface Sci.* **2004**, *279*, 137−142.
(70) Li, J.; Zeng, H. C. *Chem. Mater.* **2006**, *18*, 4270−4277.

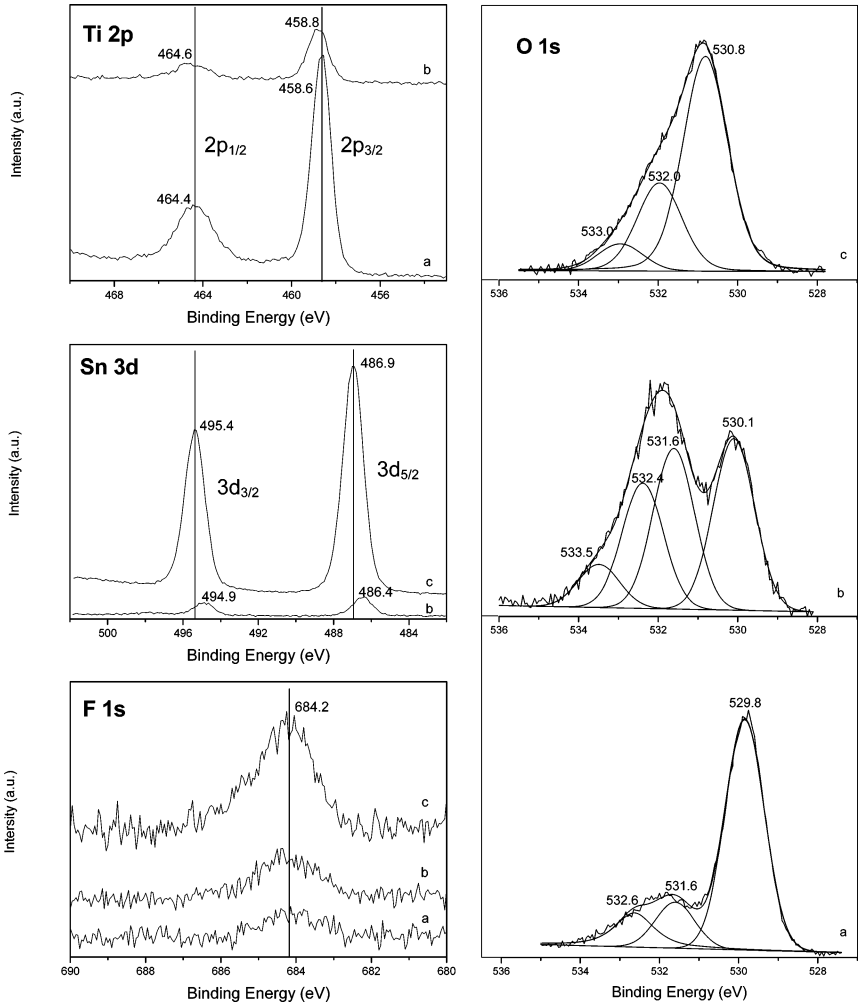

Figure 7. XPS spectra of Ti, Sn, O, and F for the $Ti_{1-x}Sn_xO_{1-0.5y}F_y$ nanospheres synthesized at 180 °C for 8 h with different amounts of SnF_4: (a) 2 mL of TiF_4 + 28 mL of H_2O, (b) 2 mL of TiF_4 + 26.6 mL of H_2O + 1.4 mL of SnF_4, and (c) 4 mL of SnF_4 + 26 mL of H_2O ([TiF_4] = 40 mM and [SnF_4] = 11.3 mM (3 days after its preparation)). Samples a, b, and c herein correspond to the samples a, d, and g of Figure 5, respectively. All XPS peak intensities are in arbitrary units (au).

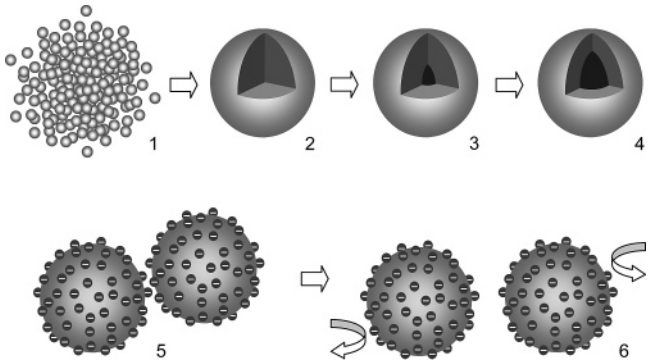

Figure 8. Formation process of hollow spheres: aggregation of nanocrystallites into solid nanospheres (1 and 2), and creation of a hollow interior via Ostwald ripening (3 and 4). While serving as a diffusion layer, surface-adsorbed fluorine anions prevent direct agglomeration of growing nanospheres (5 and 6).

observation, the content of surface fluoride anions is higher in the Sn-doped TiO_2 samples (Table 1).

Formation of these discrete oxide nanospheres can now be further addressed. As depicted in Figure 8, while sphere formation and related hollowing can be well ascribed to an Ostwald ripening process (steps 1−4), the surface-adsorbed fluoride anions will keep the nanospheres apart via negative-to-negative repulsive interaction (steps 5 to 6). Furthermore, the fluoride anion overlayer also serves as a diffusion boundary to restrain rapid crystal growth and prevent direct fusion among the nanospheres during the ripening. It is also noted that under similar processing conditions, the way and degree of solid hollowing for these nanospheres are different, depending on the content of Sn^{4+} in the solid solution. For example, homogeneous core−shell nanostructures ("homogeneous" herein means that core and shell have the same chemical constituent) can be prepared (Figure 4 and Table 1) when Sn dopant is increased in addition to the achieved spherical geometry. This observation indicates that the organizing structures of the pristine nanocrystallites in the solid aggregates vary with compositional changes in the synthesis. By controlling the composition of resultant nanospheres and therefore the agglomerative patterns of initial crystallites and dissolution properties of different metal cations of solid solutions, architectural design for the interior space can be further attained under a set of experimental parameters. Thus, investigation of the synthetic architecture of the interior space with the above aspects would become a challenging task for our future study.

As a final note of the present method, we also carried out synthetic experiments with iron dopants; the experimental details

can be found in the Supporting Information (SI-3). Similar metal-ion-doped TiO_2 nanospheres with hollow interiors can also be prepared. With a low content of dopant ions, for example, the Fe-doped TiO_2 nanospheres are in pure anatase phase. Our XPS investigation shows that iron ions adopt a trivalent chemical state (Fe^{3+}) in the mixed oxide, while F^- anions are located in the external surfaces of the oxides, similar to what has been found for the samples in Table 1. The high oxidation state of iron ions is understandable because this would ease the charge balance problem when Fe^{3+} cations substitute Ti^{4+}. The experimental details and compositional (EDX), morphological (TEM), structural (XRD), and surface (XPS) characterization results of this preliminary testing are also listed in the Supporting Information (SI-3).

Conclusions

In summary, we devised an aqueous synthetic method to fabricate hollow nanospheres of Sn^{4+}-doped anatase or rutile TiO_2 with high uniformity. Under hydrothermal conditions, the content of Sn in the mixed oxide nanospheres can be tuned by adjusting the ratio of the two starting metal fluorides TiF_4 and SnF_4. Our EDX elemental analysis shows that Sn^{4+} ions can be incorporated linearly into TiO_2 lattices, accompanied with a phase transformation from anatase to rutile, depending on the amount of dopant. Our XRD/HRTEM structural studies reveal a gradual expansion in crystal lattices upon introduction of Sn^{4+} in the binary oxides, while our XPS analysis confirms the presence of Sn−O−Ti linkages in accordance to the observed lattice expansion. On the other hand, our TEM investigation indicates that the Ostwald ripening mechanism is responsible for creation of interior spaces of the prepared oxide nanostructures. Through surface analysis it has also been further found that fluoride anions adsorbed on the surface defect sites of oxygen may serve as a diffusion layer to restrain rapid crystal growth and at the same time prevent the product nanospheres from agglomeration. As shown in our preliminary work for Fe^{3+}-deoped TiO_2 nanospheres, in principle, other metal-ion-doped oxide materials can also be prepared with the present approach. Though further development is still needed, the Ostwald ripening process can now be considered as a facile template-free alternative for preparation of hollow nanostructures, including compositionally complex materials.

Acknowledgment. The authors gratefully acknowledge the support received for this research work from grant C-534-000-004-414 from the Minerals, Metals and Materials Technology Centre (M3TC) of the National University of Singapore. J.L. would like to thank the National University of Singapore for providing her postgraduate scholarship.

Supporting Information Available: TEM image of cracked tin-doped TiO_2 nanospheres, determination of optical band gaps for some representative tin-doped TiO_2 nanospheres, and experimental details, EDX, TEM, XRD, and XPS results for iron-doped TiO_2 nanospheres (PDF). This material is available free of charge via the Internet at http://pubs.acs.org.

JA073521W